

Northumbria Research Link

Citation: Tao, Kai, Chen, Zhensheng, Yu, Jiahao, Zeng, Haozhe, Wu, Jin, Wu, Zixuan, Jia, Qingyan, Li, Peng, Fu, Yong Qing, Chang, Honglong and Yuan, Weizheng (2022) Ultra-Sensitive, Deformable and Transparent Triboelectric Tactile Sensor based on Micro-Pyramid Patterned Ionic Hydrogel for Interactive Human-Machine Interfaces. *Advanced Science*, 9 (10). p. 2104168. ISSN 2198-3844

Published by: Wiley-Blackwell

URL: <https://doi.org/10.1002/advs.202104168>
<<https://doi.org/10.1002/advs.202104168>>

This version was downloaded from Northumbria Research Link:
<http://nrl.northumbria.ac.uk/id/eprint/48172/>

Northumbria University has developed Northumbria Research Link (NRL) to enable users to access the University's research output. Copyright © and moral rights for items on NRL are retained by the individual author(s) and/or other copyright owners. Single copies of full items can be reproduced, displayed or performed, and given to third parties in any format or medium for personal research or study, educational, or not-for-profit purposes without prior permission or charge, provided the authors, title and full bibliographic details are given, as well as a hyperlink and/or URL to the original metadata page. The content must not be changed in any way. Full items must not be sold commercially in any format or medium without formal permission of the copyright holder. The full policy is available online: <http://nrl.northumbria.ac.uk/policies.html>

This document may differ from the final, published version of the research and has been made available online in accordance with publisher policies. To read and/or cite from the published version of the research, please visit the publisher's website (a subscription may be required.)



**Northumbria
University**
NEWCASTLE



UniversityLibrary

**Ultra-Sensitive, Deformable and Transparent Triboelectric
Tactile Sensor based on Micro-Pyramid Patterned Ionic Hydrogel
for Interactive Human-Machine Interfaces**

*Kai Tao¹, Zhensheng Chen¹, Jiahao Yu¹, Haozhe Zeng¹, Jin Wu², Zixuan Wu², Qingyan Jia³,
Peng Li³, Yongqing Fu⁴, Honglong Chang¹, Weizheng Yuan¹*

Prof. K. Tao, Ma. Z. Chen, Ma. J. Yu, Be. H. Zeng, Prof. H Chang, Prof. W Yuan

Ministry of Education Key Laboratory of Micro and Nano Systems for Aerospace Northwestern
Polytechnical University

Xi'an 710072, PR China

E-mail: taokai@nwpu.edu.cn; yuanwz@nwpu.edu.cn

Prof. J. Wu, Dr. Z. Wu

State Key Laboratory of Optoelectronic Materials and Technologies and the Guangdong
Province Key Laboratory of Display Material and Technology, School of Electronics and
Information Technology

Sun Yat-sen University

Guangzhou 510275, PR China

E-mail: wujin8@mail.sysu.edu.cn

Prof. Q. Jia, Prof. P. Li

Frontiers Science Center for Flexible Electronics (FSCFE), Xi'an Institute of Flexible
Electronics (IFE) & Xi'an Institute of Biomedical Materials and Engineering (IBME)

Northwestern Polytechnical University

Xi'an 710072, PR China

E-mail: iamppli@nwpu.edu.cn

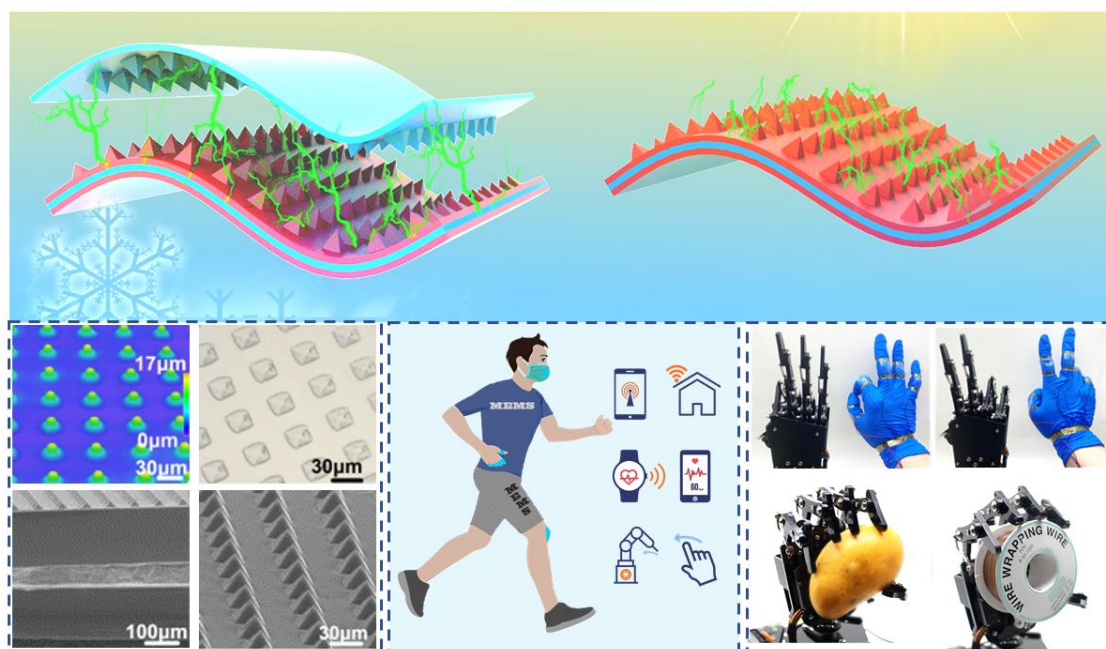
Prof. Y. Fu

Faculty of Engineering and Environment

Northumbria University

Newcastle upon Tyne, NE1 8ST, UK

TOC



Triboelectric hydrogel tactile sensor is constructed based on micro-pyramid-patterned double-network (DN) ionic organohydrogels with two working principles. This self-powered tactile sensor with wide environment tolerance and excellent sensing performance is obtained with a subtle immersion treatment and micro-pyramid-patterned method. Combining with a signal acquisition/process circuit, wearable electronics and human-machine interface applications are achieved.

Abstract

Rapid advances in wearable electronics and mechano-sensational human-machine interfaces impose great challenges in developing flexible and deformable tactile sensors with high efficiency, ultra-sensitivity, environment-tolerance and self-sustainability. Herein, we report a tactile hydrogel sensor (THS) based on micro-pyramid-patterned double-network (DN) ionic organohydrogels to detect subtle pressure changes by measuring the variations of triboelectric output signal without an external power supply. By the first time of pyramidal-patterned hydrogel fabrication method and laminated PDMS encapsulation process, the self-powered THS shows the advantages of remarkable flexibility, good transparency (~85%), and excellent sensing performance, including extraordinary sensitivity (45.97 mV Pa^{-1}), fast response (~20 ms), very low limit of detection (50 Pa) as well as high stability (36000 cycles). Moreover, with the LiBr immersion treatment method, the THS possesses excellent long-term hyper anti-freezing and anti-dehydrating properties, broad environment tolerance (-20 to 60 °C), and instantaneous peak power density of $20 \text{ }\mu\text{W cm}^{-2}$, providing reliable contact outputs with different materials and detecting very slight human motions. The THS shows no apparent output decline under the extreme environments of -29°C, 60°C and even the vacuum conditions, demonstrating the excellent application potential in the field of harsh environments. By integrating the signal acquisition/process circuit, the THS with excellent self-power sensing ability is utilized as a switching button to control electric appliances and robotic hands by simulating human finger gestures, offering its great potentials for wearable and multi-functional electronic applications.

1. Introduction

Wearable and functional electronics, especially those of ultrasensitive, transparent, flexible, and stretchable devices, are urgently demanded by human beings.^[1-7] Various wearable devices

based on mechanical sensors, flexible electronic skins, and artificial intelligence have been designed and introduced into our lives,^[8-13] promoting the rapid evolution of human sciences and technologies. Combined with the integrated circuits and human-machine interface system, the transparent, deformable, and microscale mechanical sensors demonstrate their promising prospects for the future intelligent sensor system,^[14-17] robotic manipulation,^[18-21] and digital twin applications.^[22] Different types of flexible electrodes or devices have been widely investigated for their merits of easy integration with wearable devices,^[23,24] outstanding biocompatibility,^[25] and mechanical characteristics.^[26] However, there are still many issues such as power supply limitation, environmental pollution, poor flexibility, and difficult maintainability, which severely restrict their large-scale applications in the internet of things (IoT).^[27-29] Hence, it is proposed that harvesting energy from external environments or human movements could become feasible to power such wearable sensors or devices.^[30-34]

Noticeably, triboelectric nanogenerator (TENG) has attracted enormous attention for providing considerable power sources among various energy harvesters, with merits such as simple structures, low cost, vast materials to choose from, and efficient energy conversion rates.^[35-37] Principles of the TENG coupled with triboelectrification and electrostatic induction were first proposed by Professor Zhonglin Wang's group in 2012.^[38] When two materials are contacted, electrons can migrate from one material to the other due to their different electron attraction abilities. With the continuous contact/separation of two materials induced by external stimulations, redistribution of electrons happens through using an external circuit, thus generating the alternating current and charging the small electronics. Various kinds of TENGs have been proposed to deal with the power demands of wearable and multi-functional electronics in different aspects, including 3D printed stretchable harvesters,^[30] hierarchically structured generators,^[39,40] surface-modified TENGs,^[41-44] self-powered sensors with advanced

material synthesis,^[45,46] intelligent TENGs integrated with novel digital twin acquisition technology^[6,47] and optimization of power management circuits for TENGs.^[48]

However, there are still significant challenges for these approaches:

- For example, the common electrodes used in TENGs are metals such as Cu, Al, or Au to ensure good conductivity, making the whole device rigid and opaque.^[23,49,50] Some relatively rigid while still flexible plastics (such as polyethylene terephthalate, polytetrafluoroethylene) are commonly utilized as flexible substrate.^[4] However, they often encounter difficulties for wearable and stretchable applications and bring discomfort and poor aesthetics to the human body.
- Most of the previously proposed flexible TENGs have poor environment-tolerance problems, such as severe freeze or dehydration under some extreme temperatures due to the single function materials (such as nanoparticles or liquid metal).^[30,46,51] Moreover, good transparency, high deformability, and stretchability of the devices could not be easily realized using these TENGs in wearable electronics.^[52-54]
- Due to its outstanding electron attraction ability, polydimethylsiloxane (PDMS) is widely adopted as the common triboelectric layer to acquire negative charges in TENGs.^[55-57] The PDMS films have also been considered the ideal dielectric choice for biocompatible and deformable sensors. However, plain PDMS film-based TENGs could provide a high output voltage under large external stimulation. Still, they often show a relatively low sensitivity by reason of limited contact areas, which may not be suitable enough for sensing the human physiological signals.^[1,45,58]

In recent years, hydrogels and ionic hydrogels have attracted increasing interest for their flexible electrodes applications because of their ultrahigh-stretchability, natural

biocompatibility, and excellent transparency in the visible region.^[59] Double-network (DN) hydrogel consists of two kinds of cross-linked polymer networks: three-dimensional hydrophilic polymers containing amounts of water.^[60] Therefore, the DN hydrogel demonstrates liquid-like flexibility, solid-like mechanical properties, and ionic characteristics.^[61,62] Hydrogels have been employed to fabricate various soft electronics, including sensors (e.g., strains,^[63] gases,^[64] tactile,^[65] and temperature^[12] sensors), healthcare monitoring devices,^[66] and electronic skins based on TENG technology.^[65,67,68] However, hydrogels have two significant problems in real applications. The first is the severe dehydration phenomenon when hydrogels are exposed to the external environment at a high temperature, accelerating water evaporation. The other is the solidification effect at a very low temperature caused by the freezing of water, which will significantly deteriorate the mechanical properties of the hydrogels. Great efforts have been made to improve the performance of hydrogels, such as the construction of organo-hydrogels,^[63] ionic hydrogels,^[62,69] or CNT hydrogels,^[70] which provide the inspiration of the ionic DN hydrogel in this work.

Herein, an ionic DN hydrogel using a novel lithium bromide immersion treatment (LBIT) method is produced as both the triboelectric layer and flexible electrode, providing a promising solution to achieving a hydrogel-based TENG which solve the major problems mentioned above. Functionalized polyacrylamide (Paam)/carrageenan DN hydrogel is used to realize ultrahigh-stretchability, good transparency, and high conductivity. Moreover, to achieve its low freezing point and excellent hydration ability with complimentary water, 50% LiBr saturated solution at room temperature is adopted to incorporated in the hydrogel via a facile immersion treatment strategy. As a result, the LBIT DN hydrogel displays a freezing point below -110°C and an outstanding anti-dehydrating ability, achieving good environmental tolerance of the hydrogel-based TENG sensor. Unlike the bulk hydrogel-based TENGs, which lack high

sensitivity and good flexibility, thin-film structured LBIT ionic DN hydrogel is fabricated and utilized in the tactile sensors to achieve better performance.

This work presents two kinds of triboelectric hydrogel sensors according to their different working principles: e.g., double-electrode triboelectric hydrogel sensor (DE-THS) and single-electrode triboelectric hydrogel sensor (SE-THS). Both triboelectric surfaces of the DE-THS and SE-THS are patterned with micro-pyramidal structures. Therefore, the outputs of DE-THS and SE-THS are significantly enhanced.

The newly fabricated hydrogel sensors have the following outstanding merits:

- The proposed hydrogel can be synthesized using a one-pot polymerization method which is convenient for mass production. With a simple spin-coating and bonding process, both the DE-THS and SE-THS can be obtained and show superb flexibility with an ultra-thin thickness (e.g., 640 μm for DE-THS and 400 μm for SE-THS), making it suitable for the wearable electronics applications.
- For the first time, the pyramidal-patterned hydrogel has been fabricated, and laminated PDMS encapsulation has been made. The micro-pyramidal hydrogel structures dramatically increase the contact area of the self-powered sensor, significantly increasing the sensitivity (up to 45.97 mV Pa⁻¹). Additionally, the THS shows the advantages of remarkable flexibility, transparency (~90%), and excellent sensing performance, including fast response (~20 ms), very low limit of detection (50 Pa) as well as high stability (36000 cycles).
- Multi-functional LBIT ionic DN hydrogel is used as both the flexible electrode and triboelectric layer, achieving excellent self-power functions, long-term hyper anti-freezing and anti-dehydrating properties, excellent environment tolerance (-20 to 60 °C), and instantaneous peak power density of 20 $\mu\text{W}/\text{cm}^2$ providing reliable contact outputs with different materials

and detecting very slight human motions.

- By integrating the signal acquisition/process circuit with micro pyramidal-patterned THS structures, the THS with an excellent self-power sensing ability is utilized as a switching button to control electric appliances and robotic hand by monitoring human finger gestures, offering new insights of realizing single self-powered THS for wearable and multi-functional electronic applications.

To the best of our knowledge, the micro-pyramidal structure on the hydrogel's surface is first introduced to a highly sensitive self-powered sensor. Moreover, it is the first time that the micro-structured hydrogel serves as both the flexible electrode and the friction layer opposite with the micro-structured PDMS layer, simplifying the materials composition and facilitating the mass production process. The DE-THS and SE-THS could be applied for biomechanical motion detection such as finger bending or breath sensing, which were further applied in a harsh environment for movement detection. The SE-THS is further attached to the robotic arm to detect the movements of the elbow joint under the extreme environments of -29°C , 60°C and even the vacuum conditions. Besides, combining with the customized signal acquisition/process circuit, the SE-THS could be used as a button switch to control the light's ON/OFF states and further control the robotic hand to imitate gestures, which bring the light on the development of wearable devices and electronic sensors.

2. Results and Discussion

In this research, the self-powered functions of LBIT hydrogel sensors are based on the triboelectrification mechanism, which can continuously convert the tiny forces into electric signals within a wide temperature range. As shown in **Figure 1a**, the basic architecture of DE-THS and SE-THS are assembled by combining PDMS and hydrogel membranes to achieve a highly transparent, ultra-flexible, and thin-film structure. For the DE-THS on the left-hand side

in Figure 1a, the LBIT hydrogel with micro-pyramidal structures is adopted as the top electrode and the friction layer to enable the device's higher flexibility and environmental tolerance. The micro-pyramidal structures on the hydrogel's surface can significantly increase the friction area during the triboelectrification process and thus improve the power output performance of the devices. The micro-structures on the hydrogel surface can be clearly observed from the images from a Confocal Laser Scanning Microscope (CLSM) and an optical microscope, as shown in Figures 1b and 1c, respectively. The lower sandwiched structure consists of two layers of PDMS films and an encapsulated LBIT hydrogel. The total thickness is only 400 μm , as seen from the scanning electron microscope (SEM) image (Figure 1d). The upper PDMS film with a micro-pyramidal structure as shown in the SEM image of Figure 1e is oppositely adhered to the top of the hydrogel electrode for enhancing the triboelectric effect. The micro-structured PDMS film is applied as the electrification layer to generate triboelectric charges with the contacted objects of SE-THS on the right-hand side.

Fabrication processes of both the SE-THS and DE-THS are detailed in Figure S1. Figures S2a and S2b show that the thicknesses of the DE-THS and SE-THS are 640 μm and 400 μm , respectively, demonstrating ultra-thin multilayer hydrogel structures. Figure S2c exhibits the transparency properties of both the DE-THS and SE-THS hydrogel films. The obtained transmittance spectra indicate that the DE-THS's transparency is slightly lower than those of thin-film hydrogel and SE-THS but still remains high transparency, e.g., over 85% transmittance within the wavelength range between 400 to 800 nm. Owing to the excellent optical transparency of the DE-THS, a leaf beneath the sensor could be clearly observed without any distortion (Figure 1f). Figure 1g demonstrates that the SE-THS could withstand various deformations, including stretching and twisting, with outstanding flexibility. Five SE-THSs are attached to the human knuckles to monitor the finger bending motions, which could be used to

control the robotic hand. Figure 1h demonstrates the gestures of the human hand and the corresponding movement responses of the robotic hand.

A one-pot polymerization method is introduced to synthesize the ultra-stretchable and transparent DN hydrogel, and the synthesized method is described in Figure S3 and Experiment Section. After that, 50 wt% LiBr solution is introduced in the pristine hydrogel using an immersion treatment method to avoid dehydrating and freezing because free water molecules in the pristine hydrogel can evaporate or freeze naturally due to the ambient temperature variation. Whereas after the LiBr solution immersion treatment, the water molecules in hydrogels can bond with Li^+ and Br^- ions, and the higher the degree of Li^+ and Br^- ionic hydration is, the stronger bonding strength with H^+ and O^- in water and the more bonded water molecules will be.

In consequence, the LBIT hydrogel achieves excellent anti-dehydration and anti-freezing properties (**Figure 2a**). Based on elemental analysis results from X-ray photoelectron spectroscopy (XPS) shown in Figure 2b (i and ii), high content of C (over 50%), medium content of O (about 20%), and little contents of N (near 9%) could be found in the pristine and LBIT hydrogels (See Table S1). Elements of Li and Br could also be detected in the XPS spectrum of LBIT hydrogel, which verifies the strong ionic hydration effect of LiBr (Figure 2b (iii and iv)).

To investigate the anti-freezing properties of LBIT hydrogel and pristine hydrogel, their differential scanning calorimetry (DSC) spectra were measured within a temperature range from -110 to 20°C, and the obtained results are shown in Figure 2c. The sharp peak in the spectrum at around -24.2 °C are linked to the freezing point of the pristine hydrogel. In contrast, there is no apparent DSC peak found on the spectrum of the LBIT hydrogel (Figure 2d), verifying its outstanding anti-freezing ability.

LBIT hydrogel with a polygon shape (marked in the blue region) and pristine hydrogel (in the orange region) were stored at $-40\text{ }^{\circ}\text{C}$ for 30 days. The pristine hydrogel was frozen completely, whereas the LBIT hydrogel remained unchanged (Figure 2e (i and ii)). The membrane states ($\sim 100\text{ }\mu\text{m}$ thick) of the pristine hydrogel film (in the orange area) were also stored at $-40\text{ }^{\circ}\text{C}$ for 30 days and became severely deformed and rigid. In contrast, the LBIT hydrogel film (with a similar thickness in the blue region) again remained unchanged (Figure 2e (iii and iv)), which can be attributed to the excellent low freezing point and strong hydration properties of the LBIT hydrogel. Further experiments about the anti-freezing properties of the LBIT hydrogel under extremely low temperature (-78.5°C) has been conducted. The shape evolutions of LBIT hydrogel prototypes with different LiBr percolation percentages of 15 wt%, 35 wt% and 50 wt% are recorded for 1 hour under the extremely low-temperature environment (-78.5°C). As is shown in Figure S4a, the LBIT hydrogel prototypes with LiBr percolation percentages of 15 wt% and 35 wt% are gradually frozen after storage at -78.5°C 1 hour. In contrast, the 50 wt% LiBr treated hydrogels are still kept in the gel state without any slurry, demonstrating remarkable freezing and dehydration tolerance abilities of the proposed 50 wt% LBIT hydrogel material.

In-depth evaluations for the anti-dehydrating effect of the LBIT hydrogel were also conducted. The evolutions of weight retention for both the LBIT and pristine hydrogels were recorded under different temperatures, and three groups of each sample were kept in an oven at $40\text{ }^{\circ}\text{C}$, $50\text{ }^{\circ}\text{C}$ and $60\text{ }^{\circ}\text{C}$, respectively. Due to the significant evaporation of water inside the gel, the weight of pristine hydrogel decreases rapidly and drops down to 25% within the first 8 hours (Figure 2f). Whereas the weights of LBIT hydrogel were maintained around 65%, 60%, and 58% of their original weights after being kept at $40\text{ }^{\circ}\text{C}$, $50\text{ }^{\circ}\text{C}$, and $60\text{ }^{\circ}\text{C}$, respectively (Figure 2g). A long-term dehydrating test has also been implemented. After 30 days of storage at room temperature under the ambient condition of our laboratory ($25\text{ }^{\circ}\text{C}$, 60% RH), the size of the

pristine hydrogel (N-shaped and U-shaped in the orange region) becomes much smaller and rigid, indicating its severe shrinkage (Figure 2h). In contrast, the LBIT hydrogel (P-shaped and marked in the blue region) almost keeps its original state, which is mainly due to the strong hydration ability of Li and Br. A vacuum-freeze test was also performed for these two types of samples. As shown in Figures S4c and S4d, the LBIT hydrogel was almost unchanged after one month, whereas the pristine hydrogel was frozen within 1 minute and significantly dehydrated after one month.

Further experiments have been done to investigate the humid air absorption effect of the two types of hydrogels. Figure 2i shows the weight changes of both the pristine hydrogel and LBIT hydrogel after being kept at room temperature for 60 days. The ambient humidity variation levels are recorded during this period. The weight variations of the LBIT hydrogel with the ambient humidity level were also measured, and the data are shown in Figure 2j, which have a noticeable positive correlation with the ambient humidities due to the humid air absorption effect. It is found that there are many microscale holes on the freeze-dried hydrogel surface, as shown in Figure S4b. These microscale holes play a vital role in water absorption and maintaining the dynamic weight of LBIT hydrogel. The pristine hydrogel dried thoroughly within three days. On the contrary, the LBIT hydrogel almost keeps its original state, mainly due to the LiBr's strong hydration properties. A structural optimization was calculated by using b3lyp 6-311g++ basis functions in Gaussian 09. As is demonstrated in Figure S5a and S5bs, the Li^+ and Br^- ions can form the molecular clusters with the neighboring water elements due to the strong ion-dipole interaction between ions and molecules, suppressing the formation of hydrogen bonds between the water molecules. As a result, the LBIT hydrogel exhibits an extremely low freezing point as well as an excellent hydration effect. This makes the LBIT hydrogel a suitable candidate for humidity sensing, which will be deliberated in the following sections.

Two types of interconnected networks are formed in the LBIT ionic DN hydrogel by the polymerizations of carrageenan and PAM chains. Therefore, the ionic DN hydrogel demonstrates excellent mechanical properties under loading stress, as schematically illustrated in **Figure 3a**. To evaluate its mechanical properties, tensile tests are conducted on the fabricated hydrogels. Both the pristine hydrogel and LBIT hydrogel are stretched to their maximum elongations before breaking (insets of Figure 3b). The LBIT hydrogel shows similar stretchability (up to 1488%) as that of the pristine hydrogel (1511%), and the tensile strength of pristine hydrogel is a little higher than that of the LBIT hydrogel (Figure 3b).

The stretchability and recoverability of the LBIT hydrogel are further investigated with the strain from 100% to 1000%, and the obtained results are shown in Figure 3d. There are slight hysteresis loops found at each cycle, which is mainly due to the dynamic dissociations of the physical network chains and the hydrogen bonds. Moreover, the mechanical stability of the LBIT hydrogel is studied by stretching it for five cycles under a fixed strain, which is from 100% to 700% (Figure 3e). Although there are slight decreases in the maximum stress values after each cycle, the cycling curves are generally entirely consistent during cycling deformation, demonstrating an excellent elastomer-like behavior of the LBIT hydrogel due to its double-network structure and cross-linking interactions. It shows outstanding mechanical performance at different extreme deformation situations, including punching, knotting, and twisting (Figure 3c (i to iii)). For example, no apparent damage appears on the LBIT ionic DN hydrogel surface after it is punctured by a sharp knife, as demonstrated in the inset of Figure 3c (i). It is worth noting that the LBIT hydrogel can still be stretched to 3.5 times from its original state even exposed to ambient air for as long as 2 years, as is demonstrated in Figure S5c. The enhancement of the water-retention capacity by LBIT hydrogel originates from the ion-dipole interaction between the ions such as Li^+ , Br^- and H_2O , which significantly decreased the dehydration of water molecules.

Moreover, attributing to its content of K^+ , Cl^- , Li^+ and Br^- ions, LBIT hydrogel has the ability to maintain its conductivity under various types of deformations. As exhibited in Figure 3c (iv and v), an LED is connected in series with the LBIT ionic DN hydrogel in a circuit and the applied with the current. When the hydrogel is stretched or twisted, the LED remains its bright color without apparent degradation, demonstrating its excellent conductivity in complex deformation conditions.

Attributed to the strong hydration ability of LiBr, the LBIT hydrogel could not be freeze-dried completely at $-80\text{ }^{\circ}\text{C}$ with a vacuum-freeze treatment (Figure S4d). Therefore, we use the freeze-dried pristine hydrogel for the SEM characterization (Figure S4b). The SEM image shows the highly porous structures of the hydrogel, and the interconnected porous structure provides a suitable pathway for the ions, which contributed to the excellent conductivity at different deformation conditions.

Furthermore, a strain sensor is fabricated using the LBIT ionic DN hydrogel, and its resistance changes at different strains are tested. The obtained results are shown in Figure 3f. The relative resistance change $\Delta R/R_0$ during the hydrogel deformation is calculated to evaluate the electromechanical properties of the strain sensor. R_0 is the initial resistance of the hydrogel sensor, where ΔR is its resistance variation. As is shown in Figure 3f, there is slight variation of the $\Delta R/R_0$ values for the LBIT hydrogel in the ten cyclic tests at different strains (e.g., 50%, 100%, 150%, 200%), revealing the excellent electrical stability of the LBIT hydrogel.

Dynamic resistance variations are further recorded when the LBIT hydrogel is deformed at a given strain for 2.5 s, and then the strain is increased and maintained at a higher value for another 2.5 s. This is repeated for the strain values from 0% to 335% gradually. The obtained results are shown in Figure 3e, revealing the excellent stability of the resistance values at a fixed strain for a few minutes.

Based on its excellent electric properties, a strip of LBIT ionic DN hydrogel is attached to the finger joint of a person and utilized as a strain sensor to monitor the different bending states of the finger joint (Figure 3h). The relative resistance value shows significant changes in response to the different bending angles of the finger in real-time. The larger the bending angle, the larger the values of the resistance changes. Further experiments about the anti-freezing properties of the LBIT hydrogel under extremely low temperature (-78.5°C) has been conducted. As is shown in Figure 3i, there is a slight variation of the $\Delta R/R_0$ values for the LBIT hydrogel in the five cyclic tests at different strains (e.g., 50%, 100%, 150%, 200%), revealing the excellent electrical stability of the LBIT hydrogel under the extreme cold conditions. For wearable demonstrations, the LBIT hydrogel prototypes are further attached to the fist and the elbow of a human body at such a low temperature (Figures 3j and 3k). The relative resistance value shows significant real-time changes in response to the different bending angles, demonstrating good anti-freezing properties of the LBIT hydrogel for wearable applications in an ultra-low environment. These results clearly indicate that the strip-shaped LBIT ionic DN hydrogel has excellent sensitivity and adaptability to monitor finger motions, demonstrating its good prospects for biomechanical applications.

Multilayers of DE-THS and SE-THS are further prepared by a sequence of spin coating, molding, peeling off, and final assembly process and their fabrication method demonstrated in Figure S1. They are cut to the same size of $1.5 \times 1.5 \text{ cm}^2$ for characterization. Four different types of the DE-THS devices are fabricated and characterized, including plain DE-THS (**Figure 4a**), DE-THS with pyramidal patterned PDMS and plain hydrogel (Figure 4b), pyramidal patterned hydrogel and plain PDMS (Figure 4c), both pyramidal-patterned PDMS and hydrogel (Figure 4d). Obviously, the output voltages of all types of DE-THSs increase with applied pressure initially but then reach a plateau of the maximum voltages. As shown in Figure 4a, the output voltage of the 1st DE-THS sample (e.g., plain PDMS and plain hydrogel) increases with

the applied pressure in the range of 20 Pa to 4 kPa, and the maximum output voltage of 4.5 V is obtained when the external pressure reaches its saturation pressure of 4.5 kPa. Figures 4b, 4c and 4d show that the saturation voltages is 8.5 V at a pressure of 7 kPa for the 2nd DE-THS (e.g., pyramidal patterned PDMS and plain hydrogel), 11.5 V at 4.5 kPa for the 3rd DE-THS (e.g., plain PDMS and pyramidal patterned hydrogel), 18V at 9 kPa for the 4th DE-THS (e.g., pyramidal patterned PDMS and pyramidal patterned hydrogel). The presence of both pyramidally patterned PDMS and pyramidal patterned hydrogel significantly improves the sensitivity if compared to that of the plain device, mainly due to the effectively increased contact areas and enhanced triboelectric effect.

The operating principle of the DE-THS is schematically illustrated in Figure 4e(i). When the external force is applied to the DE-THS, the top conductive hydrogel layer contacts with the bottom friction layer of the PDMS, generating electrical voltage signals due to electrostatic induction and triboelectrification effects. The triboelectric effect occurs when these two friction layers get into contact with each other, and equivalent charges with the opposite polarities could be transferred between these two contact surfaces due to the different electron affinities. Compared to that of hydrogel, PDMS has a higher electron affinity and can acquire negative charges. Once these two friction layers are separated, the hydrogel electrode will generate positive charges due to electrostatic induction. As a result, electrons will be transported to the top hydrogel electrode at the same time. An electrostatic equilibrium is achieved when these two friction layers are separated to a certain distance, above which there is no further current in the external circuit. As the upper hydrogel electrode is pressed back to contact with the bottom electrode, the process is reversed, and the currents in the opposite direction could be generated.

A theoretical model is proposed to investigate the enhanced effect of micro-structured hydrogel on the performance of fabricated DE-THS output voltage. Details of the equation derivation is shown in Section S1. For the 3rd DE-THS, the output voltage can be expressed as:

$$V_{OC} = \frac{Q}{C} = \frac{2.36\sigma A_{device\ total} \left(\frac{tp}{EL}\right)^{\frac{2}{3}}}{\epsilon A_{device\ total}/t} = 2.36 \left(\frac{\sigma t}{\epsilon}\right) \left(\frac{tp}{EL}\right)^{\frac{2}{3}} \quad (1)$$

where V_{OC} is the open-circuit voltage determined by the total triboelectric charge (Q) and the parasitic capacitance of PDMS (C); σ is the surface charge density; $A_{device\ total}$ is the total triboelectric area of the device; ϵ denotes the dielectric constant of the PDMS; p and E represent the applied pressure on the device and Young's modulus of the hydrogel, respectively; t is the thickness of the PDMS layer; L is the length of the bottom edge of the pyramidal structure.

Based on equation (1), the V_{OC} increases when a larger pressure p is applied. Due to the elastic deformation of the micro-pyramids, the contact area $A_{device\ total}$ between the PDMS and hydrogel has been increased significantly compared with that of the plain DE-THS. When the micro-pyramidal structures on the hydrogel surface are fully deformed, $A_{device\ total}$ will reach its maximum value. Thus the triboelectric effect reaches its saturated state, and the voltage will not be further increased. Therefore, the output performances of the micro-patterned DE-THS are in good agreement with the theoretical results (Figure 4c and Text S1).

It should be addressed that the voltage output of the 4th DE-THS (e.g., pyramidal patterned PDMS and pyramidal patterned hydrogel) continuously increases with the increase of pressure from 20 Pa to ~ 9 kPa. A maximum output voltage of 18 V is obtained, which shows the highest voltage value and saturation pressure among four types of DE-THSs. The dramatic output increase of the DE-THS with both the pyramidal PDMS and hydrogel is attributed to the following factors: i) The capacitance changes in the contact-deform-separate process are significantly enhanced due to the existence of air gaps and the larger dielectric constant of the PDMS. ii) Both the PDMS and hydrogel are elastomers. Therefore, the micro-pyramids can be compressed significantly, which causes a considerably increased contact area between two materials and thus more electrons generated during the contact triboelectrification process. iii)

The complex 3D morphologies on the surface of both triboelectric layers significantly reduce the adhesion effect, thus making it easier for two contact surfaces to separate, increasing the dipole moment and enhancing the output performances.

Due to the different electron acquisition abilities of the PDMS and the hydrogel, the SE-THS has been further investigated in this work. Figure 4e (ii) illustrates the basic operating principle of the SE-THS, which is based on the coupling of the triboelectric effect and electrostatic induction. A chemigum layer is used as the lower charge affinity material to contact the PDMS layer of the SE-THS. Contact electrification occurs at the interface when the chemigum layer is pressed onto the friction layer of PDMS, and equally opposite charges are generated on both sides. Since PDMS is easier to gain electrons, electrons will be transferred to PDMS from the chemigum layer. Once these two friction layers are separated, the electrons will flow back from the hydrogel electrode to balance the negative charges on PDMS. After the electrostatic equilibrium state is reached, there is no net current existed in the circuit. Once the two layers are contacted again, current in the opposite direction is detected due to the flow back of electrons. Accordingly, a cyclic alternating current output is generated by applying repeated contact–separation processes.

To further investigate the output performance of SE-THS, two types of SE-THS are fabricated, e.g., plain SE-THS and pyramidal patterned SE-THS. Similar experiments used in the tests of DE-THS have been implemented here to characterize the sensitivity of the fabricated SE-THS for the self-powered pressure sensing applications. Figure 4f shows the obtained output voltage waveforms of the plain SE-THS and the pyramidal patterned SE-THS, indicating their saturate pressure points of the output performances at around 1000 Pa and 1500 Pa, respectively. The relationship between the output voltage and applied pressure of two kinds of devices is depicted in Figure 4g. Clearly, the open-circuit voltages of both devices increase initially with the increased external pressure. However, with the further increase of the pressure, the output

voltage approaches a saturation value, which shows a similar trend with that of DE-THS. The voltage output of the pyramidal patterned SE-THS shows a much higher value compared with that of the plain SE-THS. It is worth mentioning that the pyramidal patterned SE-THS has achieved a sensitivity of 45.97 mV Pa^{-1} , which is twice as much as the 22.71 mV Pa^{-1} of unstructured SE-THS. This is mainly attributed to the presence of the proposed pyramidal microstructures, as explained before.

Furthermore, owing to the considerably large electron affinity difference between the chemigum layer and PDMS, the output voltage of the SE-THS is much higher than that of DE-THS, mainly because the chemigum easily loses electrons than the hydrogel in the triboelectric process. To find the optimal load condition of the SE-THS, the changes of output currents and voltages as well as the external resistance values are studied, and the results are shown in Figure 4h. The open-circuit voltage and short-current of pyramidal patterned SE-THS around 82 V and $83 \mu\text{A}$ can be obtained, respectively. The pyramidal patterned SE-THS exhibits a much larger output compared with those of the plain SE-THS in almost all external resistance range. Figure 4i shows that both the devices achieve their maximum power densities by using around $100 \text{ M}\Omega$ resistance load. Moreover, the pyramidally patterned SE-THS has a maximum peak power density of $\sim 20 \mu\text{W cm}^{-2}$ under 1500 Pa, which is higher than that of the plain device ($15 \mu\text{W cm}^{-2}$). Table S2 summarizes the comparisons of the-state-of-art thin-film flexible sensors with respect to operating principles, transparency, thickness, self-power operation, temperature tolerance and pressure sensitivity. It is shown that the proposed micro-pyramidal hydrogel sensor has demonstrated outstanding performance between excellent flexibility, high transparency, good sensitivity, self-powered operation and large temperature tolerance.

The pyramidal patterned SE-THS is further investigated for the identification of the most suitable materials for this application. Twelve common materials are utilized as the different triboelectric layers, including acrylic, woven cloth, microfiber cotton, polyethylene (PE), wood,

LBIT hydrogel, aluminum, fluorinated ethylene propylene (FEP), polyester fiber, copper, paper, and chemigum. As shown in **Figure 5a**, the obtained peak voltages of SE-THS using different materials are significantly different. The output performance order of each material is arranged from left to right in Figure 5a, which is just according to the quantified triboelectric series,^[71] demonstrating its effectiveness and great potential in object and material recognition application scenarios. Moreover, when the SE-THS contact with LBIT hydrogel layer (DE-THS architecture), the peak output voltage reaches ~18 V, indicating the slight polarity difference between the hydrogel and PDMS. The chemigum maintains the highest output voltage of over 50 V among the 12 different materials. As a result, SE-THS with a chemigum layer is used in further tests due to its larger output voltage.

In addition, the effect of stimulation frequency on the device's performance is also investigated, and the result is shown in Figure 5b. With the increase of the stimulation frequency, the contact status between the SE-THS device and the contacted object (chemigum is utilized in the test) changes accordingly. Results show that the output voltages increase significantly with the exciting frequencies increased from 1 to 7 Hz. When the frequency approaches 10 Hz, the output voltages become saturated. This is because as such frequency, the device and the chemigum material are fully in contact with each other, thus reaching its maximum performance of triboelectrification. However, due to the inherent mechanical limitation of the vibration system, the amplitude decreases slightly when the frequency increase while the output voltage of the signal generator is kept constant. Therefore, it is found that the output voltage of SE-THS could not monotonically increase as the frequency grows in the frequency range of 7-10 Hz. With the simple finger tapping stimulation, the transferred charge amount attends the average 4.6 nC by the SE-THS (shown in Figure S6a). The experimental result of the transferred charge (σ) can be figured out up to 2.04 nC cm^{-2} , smaller than the theoretical result (σ_0) of 5.75 nC cm^{-2} , according to the charge density expression (). It may mainly attribute to the net charge density in the dielectric layer and the decay of the electric field in the ambient condition. A modified inductance factor η is introduced to reflect the actual charge density $\sigma = \eta\sigma_0$ on the PDMS surface; here the η can be estimated as 35%.

$$\sigma = \frac{Q}{A} = \frac{4.6 \times 10^{-9}}{2.25 \times 10^{-4}} = 2.04 \text{ nC/cm}^2 \quad (2)$$

$$\sigma_0 = \frac{\varepsilon_0 \varepsilon_r V}{d} = \frac{8.85 \times 10^{-12} \times 2.6 \times 500}{200 \times 10^{-6}} = 5.75 \text{ nC/cm}^2 \quad (3)$$

where Q stands for the transferred charge amount, A is the area of the SE-THS, ε_0 is the dielectric constant of vacuum, ε_r represents the relative dielectric constant of PDMS, V is the surface potential of PDMS and d is the thickness of PDMS layer.

The response and recovery curves as a function of time are shown in Figure S6b. The fabricated SE-THS has a fast response time of 17 ms and a recovery time of 23 ms when pressed and released. Figures S6c and S6d show the stability of the SE-THS during continuous contact-release operations and the enlarged view of the obtained output voltage waveforms, respectively, demonstrating the robust stability of the proposed SE-THS after 36000 cycles of operation.

As shown in Figure 5c, the proposed THS is attached to human skins or assembled with wearable devices for the demonstration of various applications in the internet of things, healthcare monitoring, and robotic hand control. Considering the typical working conditions for using these devices, the ambient temperature in the fields usually varies from -20 °C to 60 °C. Therefore, the SE-THS is tested at -20 °C, room temperature (RT) and 60 °C, respectively, and the obtained results are shown in Figure 5d. It has been confirmed that SE-THS can perform effectively at these temperatures and a voltage output of ~16 V is generated when a simple finger pressing is applied. What is more, there is no significant drift of the outputs when the temperature changes over a wide range from -20 °C to 60 °C. Characterization results of the DE-THS samples performed in the same testing environment can be found in Figure S7, which also demonstrates the good performance and stability of the DE-THS at different temperatures.

The output voltages of the DE-THS under different relative humidity (RH) levels are further measured, and the obtained results are shown in Figure S8a. When the RH of the environment is decreased from 90% to 40%, the peak voltage is gradually increased from 2.5 V to 3.4 V

accordingly. This is mainly attributed to the excellent hydration ability of the upper hydrogel electrode/triboelectric layer in DE-THS. As the hydrogel layer continuously absorbs the moisture in the air, the triboelectrification effect between the hydrogel and PDMS will be weakened, leading to the decreased output voltage. The sensitivity of the DE-THS to the humidity level is further calculated. Based on Figure S8b, the DE-THS has an RH sensitivity of $\sim -17 \text{ mV } 1\% \text{ RH}^{-1}$ within the RH level between 40% and 90%. Hence, the device has the potential for measuring the environment humidity in the ambient.

As the thickness of the fabricated SE-THS can be reduced as thin as $400 \text{ }\mu\text{m}$, it can be applied to detect any small movements or minor stimulations. Figure 5e demonstrates the output voltage responses of the SE-THS device when the stream of water droplets continuously flow on the device's surface, and an output peak voltage of 5 V with regular waveform can be detected during water droplet flowing. Figure S9a shows the self-power generation principle during the water-PDMS contact electrification process. When the droplets contact the pyramidal patterned PDMS, triboelectrification happens on the interface between the liquid and PDMS layer. The pyramidal patterned PDMS will acquire the negative charges while the positively charged droplets flow away, leading to the alternative current between the inside hydrogel electrode and the ground. It is also found that with the increase of impinging droplets number, the value of surface potential on the original PDMS surface increases gradually and finally reaches around -500 V (Figure S9b). This can be used to detect the droplet height. Figure S9c shows the dependence of the maximum output voltage and the height of the droplet. When the droplets ($\sim 80 \text{ }\mu\text{L}$), released from a different height of 6.5 cm , 9 cm , 11 cm , 13 cm , 15 cm , 17 cm , 20 cm , the open-circuit voltage varies correspondingly. It could be observed clearly that the output voltage increases with the growth of the height initially and then obtain the highest value of 26 V approximately, providing the excellent potential for the waterdrop speed detecting ability in the future. Figure 5f shows the output signals of the DE-THS device under multiple activation

or deformation, including touching, pressing, tapping, and bending of the device, which are the four most common hand movements in our daily lives. The excitation force, frequency and compression state of the four stimulations are quite different. While touching, only the index finger at the frequency of 2 Hz was applied on the DE-THS to simulate the state of the fabricated device being touched during used for tactile sensor. Therefore, reasonable output performances have been obtained during different hand motions. These experimental results demonstrate the capability of using the DE-THS device to monitor human body movements.

The DE-THS devices are further attached to a face mask, knee, finger knuckles, and eyebrows of an operator, as shown in Figure 5g-j, respectively, in order to demonstrate the detection of the operator's motions. Figure 5g reflects the integration of the DE-THS into the inside of a face mask for potential breath sensing purposes. It is clearly seen that an output signal around 0.5 V with approximately sinusoidal waveforms is detected, with the volunteer's breathing rate only around 1.5 Hz. When attached to the operator's knee, the dynamic output signals of the DE-THS device can be obtained and perfectly match to different bending movements accordingly (Figure 5h). Figures 5i and 5j show the acquired signals from the DE-THS device from the slight movements of finger knuckles and eyebrows, respectively. As shown in Figure 5i, the DE-THS device responds well to the different bending movements of the finger knuckle. The output signal of the device at a bending angle of 90° is about 1.8 times that of 45° . As shown in Figure 5j, by attaching the SE-THS between the operator's eyebrows, the eyebrow-raising or frowning movements have generated different amplitudes of voltage signals from the device. The SE-THS is further attached to the robotic arm to detect the movements of the elbow joint (Figure 5k). The output waveforms are also recorded in the temperature of -29°C and 60°C as well as in the room-temperature vacuum conditions. As is demonstrated in Figure 5l, the SE-THS could response well to press-up movements and shows no apparent decline under

the extreme environments of -29°C , 60°C and even the vacuum conditions, demonstrating the excellent application potential in the field of harsh environments.

A human-machine interface is further established to realize the functions of button switch and robotic hand control via the intuitionistic signal-process methods. **Figure 6a** illustrates the system-level overview of the robot and light control system. The whole system contains of three main parts: (1) The THS sensors that are utilized to detect the movements of the finger joint. (2) The signal acquisition and processing system consists of Ni signal acquisition module, threshold value comparison module, signal amplifier module and driving control module. (3) The controlled terminals consist of robotic hands or LEDs. Once the THS device generates the voltage signal, the output will be received by a Ni DAQ Card (National Instrument Corporation). Peak voltage has been collected and converted into a digital signal through a LabVIEW platform. The details of the software are shown in Figure S10. Then, the pre-set threshold value comparison function will process the voltage signals into five binary signals (0/1). These signals will be processed by STM 32 amplifier module and then used to drive servo motors, which will directly drive the robotic hands to imitate the human finger gestures. A customized power amplifier is utilized to magnify the electric appliance's direct current before applying it to the devices such as an LED bulb and a robotic servo.

The proposed SE-THS has successfully demonstrated to control a button switch to operate the LED bulk for the light control system. As shown in Figure 6b, the SE-THS is used as the button switch. When the operator presses the SE-THS, the positive current generated by the contact gesture is processed by the machine interface system to switch on the LEDs. Once the pressure is released from the SE-THS, the LED lights go off immediately. When the SE-THS device is attached to the fingertip and then pressed on a surface or an object, similar but opposite control logic as that shown in Figure 6b is achieved naturally, as shown in Figure 6c. The dynamic

process for the SE-THS's controlling the button switch in two different modes can be found in the supplementary material Video S1.

We further explore the possibility of detecting human finger movements that can be applied for robot hand control. Five SE-THSs are carefully fastened by the polyimide tape on the second knuckles of each finger, providing the maximum bending angle of common hand gestures. There exist tiny gaps of around 1 millimeter between the SE-THS and chemigum gloves when the fingers are naturally straightened. Once the finger is bended, the SE-THS will contact the bottom chemigum layer to generate the voltage signal due to the basic triboelectric working principle. When the finger returns to the straight state, the opposite signal will be produced. The voltage pulses generated by the SE-THSs are utilized in five signal channels, and the SE-THSs are attached to five-finger knuckles. The obtained signals are further processed by a human-machine interface and can drive five servos to control the robot hand and mimic the motions of the operator's hand. Figure 6d demonstrates that the robot hand can accurately imitate various gestures of the human hand. The dynamic movements can be found in the supplementary material Video S2.

Figures 6e and 6f demonstrate that the robotic hands can be driven to grab a mango and a coil under the control of the SE-THS, respectively. When we made multiple gestures by moving the finger knuckles, the generated signals of five SE-THSs attached to them show quite different results as shown in Figure 6g, which proves the excellent sensitivity of the SE-THS to detect finger knuckle movements. The supplementary material Video S3 indicates that the SE-THSs attached onto the multiple fingertips have no interference of signals among each other and also without any apparent signal delays. Combined with the human-machine interface system, the SE-THS will indeed have promising prospects in surgery systems and manufacturing industries under harsh temperature conditions in the future.

3. Conclusion

In this paper, a double-network (DN) ionic LBIT hydrogel has been proposed and investigated for two types of pyramidal-patterned TENG-based hydrogel sensors, e.g., DE-THS and SE-THS. The flexible and surface pyramidal-patterned hydrogel is utilized as both the friction layer and electrode, contributing to the high transparency (around 90% in the visible range), excellent flexibility, and wide environment tolerance ($-20 \sim 60\text{ }^{\circ}\text{C}$) of the DE-THS and SE-THS. Owing to the ultra-thin thickness of the whole devices (less than 1mm), the DE-THS and SE-THS can act as tactile sensors and achieve the sensitivities of 2 mV Pa^{-1} and 45.97 mV Pa^{-1} , respectively, which have a great potential for wearable electronics and intelligent sensors. When contacted with nitrile butadiene with a simple hand pressing excitation, the SE-THS can realize a remarkable peak power density of $20\text{ }\mu\text{W cm}^{-2}$. Moreover, the unique flexible/bendable and multi-functional hydrogel and simple micro-patterned structure lead to the excellent sensitivity and compatibility of the DE-THS and SE-THS. The transparent and flexible DE-THS and SE-THS have further been applied to detect the physiological motions of a person by attaching to the joint or integrating into a mask, providing efficient and convenient methods for healthcare monitoring. The THS shows no apparent output decline under the extreme environments of -29°C , 60°C and even the vacuum conditions, demonstrating the excellent application potential in the field of harsh environments. By further combining DE-THS and SE-THS with a signal acquisition/process circuit, the sensors demonstrate their good ability as a flexible switch button to control the electric appliance and robotic hand movements by monitoring human fingers' gestures. The research outcomes successfully demonstrate the versatility and viability of the DN ionic LBIT hydrogel and DE-THS/SE-THS for real-world self-powered wearable and interactive human-machine interface applications

4. Experimental Section/Methods

Materials and characterization: Carrageenan, acrylamide, N'-Methylenebis (acrylamide) (MBA), ammonium persulfate (AP), KCl, and acrylamide (AM) are obtained from Aladdin. The 99% lithium bromide is purchased from Sigma-Aldrich. Polydimethylsiloxane (PDMS Sylgard 184) is bought from Dow Corning Inc. The 0.05mm Ag wire is purchased from QingHe Silver Jewelry Corporation, and applied as the conductive fabric. Double sticky tapes used in this research are purchased from 3M Corporation. All reagents in this work are used in as-received conditions without any refinement.

The transmittance of the hydrogel and DE-THS/SE-THS is tested using a UV-Vis spectrometer (Shimadzu UV-1780). The DSC spectra of pristine hydrogel and LBIT hydrogel are measured by using a PerkinElmer DSC 8500, with the cooling process from 20 to -115 °C at a rate of 10°C/min. XPS spectra of pristine hydrogel and LBIT hydrogel are obtained using Thermo Escalab 250Xi XPS, Thermo Fisher Scientific Inc. Micro-structures of the samples are observed using a scanning electron microscope (SEM, VEGA 3 LMU). Because the LiBr exists in the LBIT hydrogels, they cannot be freeze-dried completely. Thus, we choose the pristine hydrogel to coat the gold for the SEM images. Confocal Laser Scanning Microscope (CLSM) image of the micro-patterned hydrogel is acquired using the OLS 5100 Olympus. The mechanical tensile tests are performed on IBTC-300SL tensile tester, Care Tianjin Corporation at a constant speed of 100mm/min. The Futek wiring code (WC1) was applied to measure the external force of excitation, and a mechanical shaker triggered the periodic stimulations on the DE-THS and SE-THS. The resistance variations of the hydrogels are measured with a digital multimeter (Keithley DMM6500). To record the output signal of the self-powered sensor, the high-impedance data acquisition system (NI USB-6289 DAQ Card) is utilized in the testing platform. The surface potential of PDMS is detected by surface potential scanner (Trek Model 347 USA). The transferred charge is measured using electrometers system (Keithley 6514).

Preparation of micro-pyramidal patterned PDMS films: The pre-polymer and curing agents of PDMS are mixed at the ratio of 10:1 to prepare the PDMS solution. Then the pre-cured solution is vacuum treated (-0.06 MPa for 30 mins) to remove the air bubble inside. The uncured PDMS precursor is spin-coated (800 rpm/min for the 30s) on a micro-pyramidal patterned silicon wafer to realize the thickness around $200\text{ }\mu\text{m}$ and cured on the oven at $70\text{ }^{\circ}\text{C}$ for 2 h to form the micro-pyramidal patterned PDMS.

Preparation of micro-pyramidal patterned LBIT hydrogel film: A one-pot polymerization method is used to synthesize the hydrogels. In the first phase, 41.0 g of deionized water with 0.005 g of MBA, 7.5 g of AM, 0.09 g of KCl, and 1.5 g of carrageenan are added into a container and magnetically stirred under the oil bath at 95°C for 5 hours. After that, the whole solution is cooled down to $75\text{ }^{\circ}\text{C}$ and 0.0375 g of AP is subsequently added inside. The solution is stirred for several minutes and poured on the micro-inverted pyramidal etched silicon wafer, followed by the spin coating method. Hydrogel film on the wafer is then kept at $6\text{ }^{\circ}\text{C}$ for 1 hour to format the carrageenan and heated to $95\text{ }^{\circ}\text{C}$ for another hour to cross-link the PAM. In the last step, the hydrogel film is immersed in the 50 wt% LiBr solution for 2 hours to obtain the LBIT hydrogel with the micro-pyramidal patterns.

Preparation of the SE-THS: The as-prepared micro-pyramidal patterned PDMS films on the silicon wafer are utilized on the bottom PDMS substrate. After added AP into the hydrogel precursor solution and kept stirring at $75\text{ }^{\circ}\text{C}$ for 1 min, the mixed hydrogel solution is poured on the PDMS and spin-coated to form a thin film. The as-prepared hydrogel film on the PDMS layer is kept at $6\text{ }^{\circ}\text{C}$ for 1 hour and heated to $95\text{ }^{\circ}\text{C}$ for another hour for solidification. After the LBIT formation, the as-formed hydrogel is cut into the square electrode, and a silver wire electrode is attached to the surface of this film. Another thin film of PDMS is spin-coated and cured on the hydrogel to further encapsulate it to form the whole SE-THS.

Preparation of the DE-THS: For fabrication of the DE-THS, the micro-pyramidal patterned hydrogel is adhered to the SE-THS using a double sticky tape to ensure the micro-patterned surfaces of hydrogel and PDMS are located at the opposite position. The DE-THS is then fabricated by connecting the electrical tester between the two silver wires in the top and bottom hydrogel electrodes.

Study Participation: Prior to participation in the experiments, informed consent was obtained from the volunteer in all experiments.

Supporting Information

Supporting Information is available from the Wiley Online Library or from the author.

Data Availability

The data sets generated and analyzed in this study are available from the corresponding author upon request.

Acknowledgements

This research is supported by the National Natural Science Foundation of China Grant (No. 51705429 & No. 61801525), the Fundamental Research Funds for the Central Universities, Guangdong Natural Science Funds Grant (2018A030313400), Space Science and Technology Foundation, Shenzhen Research Plan (JCYJ20180306171637410), 111 Project No. B13044, UK Engineering and Physical Sciences Research Council (EPSRC) for support under grant EP/P018998/1, International Exchange Grant (IEC/NSFC/201078) through Royal Society UK and the NSFC.

Conflict of Interest

The authors declare no competing interests.

Keywords

Flexible electronics, Triboelectric tactile sensor, Self-powered hydrogel sensor, Human-machine interface, Pyramidal-patterned hydrogel

Received: ((will be filled in by the editorial staff))

Revised: ((will be filled in by the editorial staff))

Published online: ((will be filled in by the editorial staff))

References

- [1] Y. Jiang, K. Dong, X. Li, J. An, D. Wu, X. Peng, J. Yi, C. Ning, R. Cheng, P. YuZ. L. Wang. Stretchable, Washable, and Ultrathin Triboelectric Nanogenerators as Skin - Like Highly Sensitive Self - Powered Haptic Sensors. *Adv. Funct. Mater.*, **2020**, *31*, 2005584.
- [2] Z. Wang, L. Chen, Y. Chen, P. Liu, H. DuanP. Cheng. 3D Printed Ultrastretchable, Hyper-Antifreezing Conductive Hydrogel for Sensitive Motion and Electrophysiological Signal Monitoring. *Research (Wash D C)*, **2020**, *2020*, 1426078.
- [3] G. Cai, J. Wang, K. Qian, J. Chen, S. LiP. S. Lee. Extremely Stretchable Strain Sensors Based on Conductive Self-Healing Dynamic Cross-Links Hydrogels for Human-Motion Detection. *Adv Sci (Weinh)*, **2017**, *4*, 1600190.
- [4] K. Tao, Z. Chen, H. Yi, R. Zhang, Q. Shen, J. Wu, L. Tang, K. Fan, Y. Fu, J. MiaoW. Yuan. Hierarchical Honeycomb-Structured Electret/Triboelectric Nanogenerator for Biomechanical and Morphing Wing Energy Harvesting. *Nano-Micro Letters*, **2021**, *13*.
- [5] K. Dong, X. PengZ. L. Wang. Fiber/Fabric-Based Piezoelectric and Triboelectric Nanogenerators for Flexible/Stretchable and Wearable Electronics and Artificial Intelligence. *Adv. Mater.*, **2020**, *32*, e1902549.
- [6] G. Li, S. Liu, L. WangR. Zhu. Skin-inspired quadruple tactile sensors integrated on a robot hand enable object recognition. *Sci Robot*, **2020**, *5*.
- [7] Z. Jiao, C. Zhang, W. Wang, M. Pan, H. YangJ. Zou. Advanced Artificial Muscle for Flexible Material - Based Reconfigurable Soft Robots. *Advanced Science*, **2019**, *6*, 1901371.
- [8] X. Chen, Y. Wu, J. Shao, T. Jiang, A. Yu, L. XuZ. L. Wang. On-Skin Triboelectric Nanogenerator and Self-Powered Sensor with Ultrathin Thickness and High Stretchability. *Small*, **2017**, *13*.

- [9] X. S. Zhang, M. D. Han, B. Kim, J. F. Bao, J. BruggerH. X. Zhang. All-in-one self-powered flexible microsystems based on triboelectric nanogenerators. *Nano Energy*, **2018**, *47*, 410.
- [10] J. Yu, X. Hou, M. Cui, S. Zhang, J. He, W. Geng, J. MuX. Chou. Highly skin-conformal wearable tactile sensor based on piezoelectric-enhanced triboelectric nanogenerator. *Nano Energy*, **2019**, *64*, 103923.
- [11] K. Tao, H. Yi, Y. Yang, H. Chang, J. Wu, L. Tang, Z. Yang, N. Wang, L. Hu, Y. Fu, J. MiaoW. Yuan. Origami-inspired electret-based triboelectric generator for biomechanical and ocean wave energy harvesting. *Nano Energy*, **2020**, *67*, 104197.
- [12] Z. Wu, H. Ding, K. Tao, Y. Wei, X. Gui, W. Shi, X. XieJ. Wu. Ultrasensitive, Stretchable, and Fast-Response Temperature Sensors Based on Hydrogel Films for Wearable Applications. *ACS Appl Mater Interfaces*, **2021**, *13*, 21854.
- [13] H. Zhang, J. Guo, Y. Wang, L. SunY. Zhao. Stretchable and Conductive Composite Structural Color Hydrogel Films as Bionic Electronic Skins. *Adv Sci (Weinh)*, **2021**, e2102156.
- [14] Y. Wang, H. Wu, L. Xu, H. Zhang, Y. YangZ. L. Wang. Hierarchically patterned self-powered sensors for multifunctional tactile sensing. *Sci Adv*, **2020**, *6*, eabb9083.
- [15] M. Zhu, Z. Sun, Z. Zhang, Q. Shi, T. He, H. Liu, T. ChenC. Lee. Haptic-feedback smart glove as a creative human-machine interface (HMI) for virtual/augmented reality applications. *Sci Adv*, **2020**, *6*, eaaz8693.
- [16] K. Tao, H. P. Yi, L. H. Tang, J. Wu, P. H. Wang, N. Wang, L. X. Hu, Y. Q. Fu, J. M. MiaoH. L. Chang. Piezoelectric ZnO thin films for 2DOF MEMS vibrational energy harvesting. *Surf Coat Tech*, **2019**, *359*, 289.
- [17] M. Fu, J. Zhang, Y. Jin, Y. Zhao, S. HuangC. F. Guo. A Highly Sensitive, Reliable, and High-Temperature-Resistant Flexible Pressure Sensor Based on Ceramic Nanofibers. *Adv Sci (Weinh)*, **2020**, *7*, 2000258.

- [18] L. Tang, J. ShangX. Jiang. Multilayered electronic transfer tattoo that can enable the crease amplification effect. *Sci Adv*, **2021**, 7.
- [19] T. Jin, Z. Sun, L. Li, Q. Zhang, M. Zhu, Z. Zhang, G. Yuan, T. Chen, Y. Tian, X. HouC. Lee. Triboelectric nanogenerator sensors for soft robotics aiming at digital twin applications. *Nat Commun*, **2020**, 11, 5381.
- [20] T. He, Q. Shi, H. Wang, F. Wen, T. Chen, J. OuyangC. Lee. Beyond energy harvesting - multi-functional triboelectric nanosensors on a textile. *Nano Energy*, **2019**, 57, 338.
- [21] X. Pu, H. Guo, Q. Tang, J. Chen, L. Feng, G. Liu, X. Wang, Y. Xi, C. HuZ. L. Wang. Rotation sensing and gesture control of a robot joint via triboelectric quantization sensor. *Nano Energy*, **2018**, 54, 453.
- [22] B. Dong, Q. Shi, Y. Yang, F. Wen, Z. ZhangC. Lee. Technology evolution from self-powered sensors to AIoT enabled smart homes. *Nano Energy*, **2021**, 79, 105414.
- [23] K. Tao, H. P. Yi, Y. Yang, L. H. Tang, Z. S. Yang, J. Wu, H. L. ChangW. Z. Yuan. Miura-origami-inspired electret/triboelectric power generator for wearable energy harvesting with water-proof capability. *Microsyst Nanoeng*, **2020**, 6.
- [24] A. R. Chowdhury, A. M. Abdullah, U. V. Romero, I. Hussain, C. Olivares, S. Danti, J. LiM. J. Uddin. Decentralized triboelectric electronic health monitoring flexible microdevice. *Medical Devices & Sensors*, **2020**, 3.
- [25] T. Li, L. Li, H. Sun, Y. Xu, X. Wang, H. Luo, Z. LiuT. Zhang. Porous Ionic Membrane Based Flexible Humidity Sensor and its Multifunctional Applications. *Adv Sci (Weinh)*, **2017**, 4, 1600404.
- [26] X. Zhou, K. Parida, O. Halevi, Y. Liu, J. Xiong, S. MagdassiP. S. Lee. All 3D-printed stretchable piezoelectric nanogenerator with non-protruding kirigami structure. *Nano Energy*, **2020**, 72, 104676.
- [27] Y. Zhou, W. Deng, J. XuJ. Chen. Engineering Materials at the Nanoscale for Triboelectric Nanogenerators. *Cell Reports Physical Science*, **2020**, 1, 100142.

- [28] D. Zhang, D. Wang, Z. Xu, X. Zhang, Y. Yang, J. Guo, B. ZhangW. Zhao. Diversiform sensors and sensing systems driven by triboelectric and piezoelectric nanogenerators. *Coord. Chem. Rev.*, **2021**, 427, 213597.
- [29] K. Parida, J. Xiong, X. ZhouP. S. Lee. Progress on triboelectric nanogenerator with stretchability, self-healability and bio-compatibility. *Nano Energy*, **2019**, 59, 237.
- [30] K. Parida, G. Thangavel, G. Cai, X. Zhou, S. Park, J. XiongP. S. Lee. Extremely stretchable and self-healing conductor based on thermoplastic elastomer for all-three-dimensional printed triboelectric nanogenerator. *Nat Commun*, **2019**, 10, 2158.
- [31] Y. Song, J. Min, Y. Yu, H. Wang, Y. Yang, H. ZhangW. Gao. Wireless battery-free wearable sweat sensor powered by human motion. *Sci Adv*, **2020**, 6.
- [32] X. S. Zhang, M. D. Han, R. X. Wang, F. Y. Zhu, Z. H. Li, W. WangH. X. Zhang. Frequency-multiplication high-output triboelectric nanogenerator for sustainably powering biomedical microsystems. *Nano Lett.*, **2013**, 13, 1168.
- [33] Q. Liu, Z. Liu, C. Li, K. Xie, P. Zhu, B. Shao, J. Zhang, J. Yang, J. Zhang, Q. WangC. F. Guo. Highly Transparent and Flexible Iontronic Pressure Sensors Based on an Opaque to Transparent Transition. *Adv Sci (Weinh)*, **2020**, 7, 2000348.
- [34] X. Xia, J. FuY. Zi. A universal standardized method for output capability assessment of nanogenerators. *Nat Commun*, **2019**, 10, 4428.
- [35] Z. Ren, Q. Zheng, H. Wang, H. Guo, L. Miao, J. Wan, C. Xu, S. ChengH. Zhang. Wearable and self-cleaning hybrid energy harvesting system based on micro/nanostructured haze film. *Nano Energy*, **2020**, 67, 104243.
- [36] X. S. Zhang, M. D. Han, B. MengH. X. Zhang. High performance triboelectric nanogenerators based on large-scale mass-fabrication technologies. *Nano Energy*, **2015**, 11, 304.

- [37] B. N. Chandrashekar, B. Deng, A. S. Smitha, Y. Chen, C. Tan, H. Zhang, H. PengZ. Liu. Roll-to-Roll Green Transfer of CVD Graphene onto Plastic for a Transparent and Flexible Triboelectric Nanogenerator. *Adv. Mater.*, **2015**, 27, 5210.
- [38] F. R. Fan, Z. Q. TianZ. L. Wang. Flexible triboelectric generator! *Nano Energy*, **2012**, 1, 328.
- [39] X. Chen, Y. Song, Z. Su, H. Chen, X. Cheng, J. Zhang, M. HanH. Zhang. Flexible fiber-based hybrid nanogenerator for biomechanical energy harvesting and physiological monitoring. *Nano Energy*, **2017**, 38, 43.
- [40] G. Li, D. Chen, C. Li, W. LiuH. Liu. Engineered Microstructure Derived Hierarchical Deformation of Flexible Pressure Sensor Induces a Supersensitive Piezoresistive Property in Broad Pressure Range. *Adv Sci (Weinh)*, **2020**, 7, 2000154.
- [41] S. Gong, J. Zhang, C. Wang, K. RenZ. L. Wang. A Monocharged Electret Nanogenerator - Based Self - Powered Device for Pressure and Tactile Sensor Applications. *Adv. Funct. Mater.*, **2019**, 29, 1807618.
- [42] X. Chen, J. Xiong, K. Parida, M. Guo, C. Wang, C. Wang, X. Li, J. ShaoP. S. Lee. Transparent and stretchable bimodal triboelectric nanogenerators with hierarchical micro-nanostructures for mechanical and water energy harvesting. *Nano Energy*, **2019**, 64, 103904.
- [43] X. Li, C. Xu, C. Wang, J. Shao, X. Chen, C. Wang, H. Tian, Y. Wang, Q. Yang, L. WangB. Lu. Improved triboelectrification effect by bendable and slidable fish-scale-like microstructures. *Nano Energy*, **2017**, 40, 646.
- [44] F. Liang, X. J. Zhao, H. Y. Li, Y. J. Fan, J. W. Cao, Z. L. WangG. Zhu. Stretchable shape-adaptive liquid-solid interface nanogenerator enabled by in-situ charged nanocomposite membrane. *Nano Energy*, **2020**, 69, 104414.
- [45] J. Xiong, G. Thangavel, J. Wang, X. ZhouP. S. Lee. Self-healable sticky porous elastomer for gas-solid interacted power generation. *Sci Adv*, **2020**, 6, eabb4246.

- [46] Y. Yang, J. Han, J. Huang, J. Sun, Z. L. Wang, S. SeoQ. Sun. Stretchable Energy - Harvesting Tactile Interactive Interface with Liquid - Metal - Nanoparticle - Based Electrodes. *Adv. Funct. Mater.*, **2020**, *30*, 1909652.
- [47] Q. ShiC. Lee. Self-Powered Bio-Inspired Spider-Net-Coding Interface Using Single-Electrode Triboelectric Nanogenerator. *Adv Sci (Weinh)*, **2019**, *6*, 1900617.
- [48] S. Xu, L. Zhang, W. Ding, H. Guo, X. WangZ. L. Wang. Self-doubled-rectification of triboelectric nanogenerator. *Nano Energy*, **2019**, *66*, 104165.
- [49] M. Muthu, R. Pandey, X. Wang, A. Chandrasekhar, I. A. PalaniV. Singh. Enhancement of triboelectric nanogenerator output performance by laser 3D-Surface pattern method for energy harvesting application. *Nano Energy*, **2020**, *78*, 105205.
- [50] B. Meng, W. Tang, Z. H. Too, X. S. Zhang, M. D. Han, W. LiuH. X. Zhang. A transparent single-friction-surface triboelectric generator and self-powered touch sensor. *Energ Environ Sci*, **2013**, *6*, 3235.
- [51] H. Peng, Y. Xin, J. Xu, H. LiuJ. Zhang. Ultra-stretchable hydrogels with reactive liquid metals as asymmetric force-sensors. *Materials Horizons*, **2019**, *6*, 618.
- [52] J. Wu, Z. Wu, W. Huang, X. Yang, Y. Liang, K. Tao, B. R. Yang, W. ShiX. Xie. Stretchable, Stable, and Room-Temperature Gas Sensors Based on Self-Healing and Transparent Organohydrogels. *ACS Appl Mater Interfaces*, **2020**, *12*, 52070.
- [53] Y. Song, H. Chen, Z. Su, X. Chen, L. Miao, J. Zhang, X. ChengH. Zhang. Highly Compressible Integrated Supercapacitor-Piezoresistance-Sensor System with CNT-PDMS Sponge for Health Monitoring. *Small*, **2017**, *13*.
- [54] H. Sun, Y. Zhao, S. Jiao, C. Wang, Y. Jia, K. Dai, G. Zheng, C. Liu, P. WanC. Shen. Environment Tolerant Conductive Nanocomposite Organohydrogels as Flexible Strain Sensors and Power Sources for Sustainable Electronics. *Adv. Funct. Mater.*, **2021**, 2101696.

- [55] X. Pu, M. Liu, X. Chen, J. Sun, C. Du, Y. Zhang, J. Zhai, W. HuZ. L. Wang. Ultrastretchable, transparent triboelectric nanogenerator as electronic skin for biomechanical energy harvesting and tactile sensing. *Sci Adv*, **2017**, *3*, e1700015.
- [56] F. R. Fan, L. Lin, G. Zhu, W. Wu, R. ZhangZ. L. Wang. Transparent triboelectric nanogenerators and self-powered pressure sensors based on micropatterned plastic films. *Nano Lett.*, **2012**, *12*, 3109.
- [57] X. F. Zhao, C. Z. Hang, H. L. Lu, K. Xu, H. Zhang, F. Yang, R. G. Ma, J. C. WangD. W. Zhang. A skin-like sensor for intelligent Braille recognition. *Nano Energy*, **2020**, *68*, 104346.
- [58] M. Shi, J. Zhang, H. Chen, M. Han, S. A. Shankaregowda, Z. Su, B. Meng, X. ChengH. Zhang. Self-Powered Analogue Smart Skin. *ACS Nano*, **2016**, *10*, 4083.
- [59] Y. S. ZhangA. Khademhosseini. Advances in engineering hydrogels. *Science*, **2017**, *356*.
- [60] J. Wu, S. Han, T. Yang, Z. Li, Z. Wu, X. Gui, K. Tao, J. Miao, L. K. Norford, C. LiuF. Huo. Highly Stretchable and Transparent Thermistor Based on Self-Healing Double Network Hydrogel. *ACS Appl Mater Interfaces*, **2018**, *10*, 19097.
- [61] Y. Bai, B. Chen, F. Xiang, J. Zhou, H. WangZ. Suo. Transparent hydrogel with enhanced water retention capacity by introducing highly hydratable salt. *Appl. Phys. Lett.*, **2014**, *105*, 151903.
- [62] D. Lou, C. Wang, Z. He, X. Sun, J. LuoJ. Li. Robust organohydrogel with flexibility and conductivity across the freezing and boiling temperatures of water. *Chem Commun (Camb)*, **2019**, *55*, 8422.
- [63] Z. HeW. Yuan. Adhesive, Stretchable, and Transparent Organohydrogels for Antifreezing, Antidrying, and Sensitive Ionic Skins. *ACS Appl Mater Interfaces*, **2021**, *13*, 1474.
- [64] J. Wu, Z. Wu, S. Han, B. R. Yang, X. Gui, K. Tao, C. Liu, J. MiaoL. K. Norford. Extremely Deformable, Transparent, and High-Performance Gas Sensor Based on Ionic Conductive Hydrogel. *ACS Appl Mater Interfaces*, **2019**, *11*, 2364.

- [65] T. Jing, B. Xu, Y. Yang, M. LiY. Gao. Organogel electrode enables highly transparent and stretchable triboelectric nanogenerators of high power density for robust and reliable energy harvesting. *Nano Energy*, **2020**, 78, 105373.
- [66] J.-N. Kim, J. Lee, H. LeeI.-K. Oh. Stretchable and self-healable catechol-chitosan-diatom hydrogel for triboelectric generator and self-powered tremor sensor targeting at Parkinson disease. *Nano Energy*, **2021**, 82, 105705.
- [67] L. B. Huang, X. Y. Dai, Z. H. Sun, M. C. Wong, S. Y. Pang, J. C. Han, Q. Q. Zheng, C. H. Zhao, J. KongJ. H. Hao. Environment-resisted flexible high performance triboelectric nanogenerators based on ultrafast self-healing non-drying conductive organohydrogel. *Nano Energy*, **2021**, 82, 105724.
- [68] Y. Wang, L. ZhangA. Lu. Highly stretchable, transparent cellulose/PVA composite hydrogel for multiple sensing and triboelectric nanogenerators. *Journal of Materials Chemistry A*, **2020**, 8, 13935.
- [69] X. Lu, L. Zheng, H. Zhang, W. Wang, Z. L. WangC. Sun. Stretchable, transparent triboelectric nanogenerator as a highly sensitive self-powered sensor for driver fatigue and distraction monitoring. *Nano Energy*, **2020**, 78, 105359.
- [70] S. Han, C. Liu, X. Lin, J. Zheng, J. WuC. Liu. Dual Conductive Network Hydrogel for a Highly Conductive, Self-Healing, Anti-Freezing, and Non-Drying Strain Sensor. *ACS Applied Polymer Materials*, **2020**, 2, 996.
- [71] H. Zou, Y. Zhang, L. Guo, P. Wang, X. He, G. Dai, H. Zheng, C. Chen, A. C. Wang, C. XuZ. L. Wang. Quantifying the triboelectric series. *Nat Commun*, **2019**, 10, 1427.

Figure Captions

Figure 1. Structure design of the DE-THS and SE-THS: (a) Schematic diagram showing the detailed structures, anti-dehydrating and anti-freezing properties of the ultra-deformable DE-THS and SE-THS. (b-c) CLSM image and optical microscope photograph of the micro-pyramid structure on hydrogel surface. (d) Cross-section SEM of the SE-THS. (e) SEM image of the micro-pyramid structure on the PDMS. (f) Optical image of the DE-THS. (g) Optical images of original, stretching, and twisting of SE-THS. (h) Demonstrations of the robotic hand gestures corresponding to four different hand motions based on the SE-THS.

Figure 2. Anti-dehydrating and anti-freezing properties of the hydrogel: (a) Schematic illustration shows the molecular architecture, anti-dehydrating and anti-freezing characteristics of pristine hydrogel and LiBr immersion treated (LBIT) hydrogel. (b) XPS spectra of i) pristine hydrogel ii) LBIT hydrogel iii) Br 3d and iv) Li 1s, respectively. (c) and (d) DSC measurement of the pristine hydrogel and LBIT hydrogel. (e) Anti-freezing properties of the pristine hydrogel (in orange region) and the LBIT hydrogel (marked in blue region) in different shapes stored at -40 °C for 30 days. (f) Comparison of weight retention of the pristine hydrogel under 40, 50 and 60 °C at 30% RH. (g) Comparison of the anti-dehydrating properties of LBIT hydrogel under 40, 50 and 60 °C at 30% RH. (h) Anti-dehydrating property of the pristine hydrogel (N-shaped and U-shaped in the orange region) and LBIT hydrogel (P-shaped and marked in the blue region) after exposure at RT for 30 days. (i) Weight change of pristine hydrogel and LBIT hydrogel after being kept at RT for 60 days and the ambient humidity variation during this period. (j) Relationship between the weight retention and relative humidity of the LBIT hydrogel.

Figure 3. Electromechanical properties of the double-network LBIT hydrogel: (a) Schematic illustration shows the Double-Network (DN) architecture of the PAM chain and the Carrageenan chain in the hydrogel. (b) Strain-stress curves of pristine hydrogel and LBIT hydrogel. (c) Mechanical deformability and conductivity of the LBIT hydrogel. (d) Stretching and releasing tests from 100% to 1000% of LBIT hydrogel. (e) Cyclic test of the LBIT hydrogel under 100% to 700% stretching states. (f) Comparison of dynamic resistance of 10 cycles

between different deformations sequentially, including 50%, 100%, 150%, 200% strain. (g) Relative resistance variation versus strains from 0% to 335%. (h) Real-time responses of the LBIT hydrogel to different bending states when attached to the index finger. (i) The resistance variations ($\Delta R/R_0$) at cyclic strains after storing at the temperature of -78.5°C . (j) The long-term durability test of the LBIT hydrogel after being stored at -78.5°C for 1 h. (k) Resistance variation curves of the LBIT hydrogel on the fist and the elbow of a human body at different bending angles.

Figure 4. The basic principles, characterizations and performances of DE-THS and SE-THS: (a-d) Open-circuit voltage variation under different pressures of four kinds of DE-THS: (a) Plain PDMS-Plain Hydrogel; (b) Pyramidal Patterned PDMS-Plain Hydrogel; (c) Plain PDMS-Pyramidal Patterned Hydrogel; (d) Pyramidal Patterned PDMS-Pyramidal Patterned Hydrogel. (e) Schematic illustration of the working principle of DE-THS and SE-THS. (f) Voltage curves under different applied pressures of plain SE-THS and pyramidal patterned SE-THS. (g) Open-circuit voltage variation under different pressures of plain SE-THS and pyramidal patterned SE-THS. (h) Dependence of the output on the external resistance load of plain SE-THS and pyramidal patterned SE-THS. (i) Dependence of the power density on the resistance of external load of plain SE-THS and pyramidal patterned SE-THS.

Figure 5. Diversified applications of DE-THS and SE-THS: (a) Open-circuit voltage of the SE-THS under contact-separation motion with different materials at 1 Hz by finger tapping; (b) The open-circuit voltage variation of SE-THS at various applied frequencies by vibration table; (c) Schematic diagram of the applications of the proposed SE-THS: IoT, healthcare monitoring and robot control; (d) Output voltage of the SE-THS at different temperatures by finger tapping; (e) Open circuit voltage of the SE-THS in water drop sensing; (f) Output signals under touching, pressing, tapping and bending; (g)-(j) Applications of SE-THS on human motion detection: (g) Eyebrow movement; (h) Breathing monitor; (i) Knee joint motion; (j) Knuckle movement; (k) Attach the SE-THS onto the robotic arm to detect the movements of the elbow joint; (l) The testing environment of the LBIT hydrogel sensor in the temperature of -29°C and 60°C as well as in the vacuum condition.

Figure 6. The implementation of SE-THS for interactive human-machine interfaces application: (a) Schematic diagram of the robot hand control and light control system; (b) Output signal of SE-THS attached to the table when serving as a light switch; (c) Output signal of SE-THS attached to the knuckles when serving as a light switch; (d) The photographs of human hand gestures and corresponding robot hand motions; (e) The photograph of grabbing a mango by robot hand; (f) The photograph of grabbing a coil by robot hand; (g) Generated outputs from five sensors: thumb, index finger, middle finger, ring finger and pinky finger when fingers move successively.

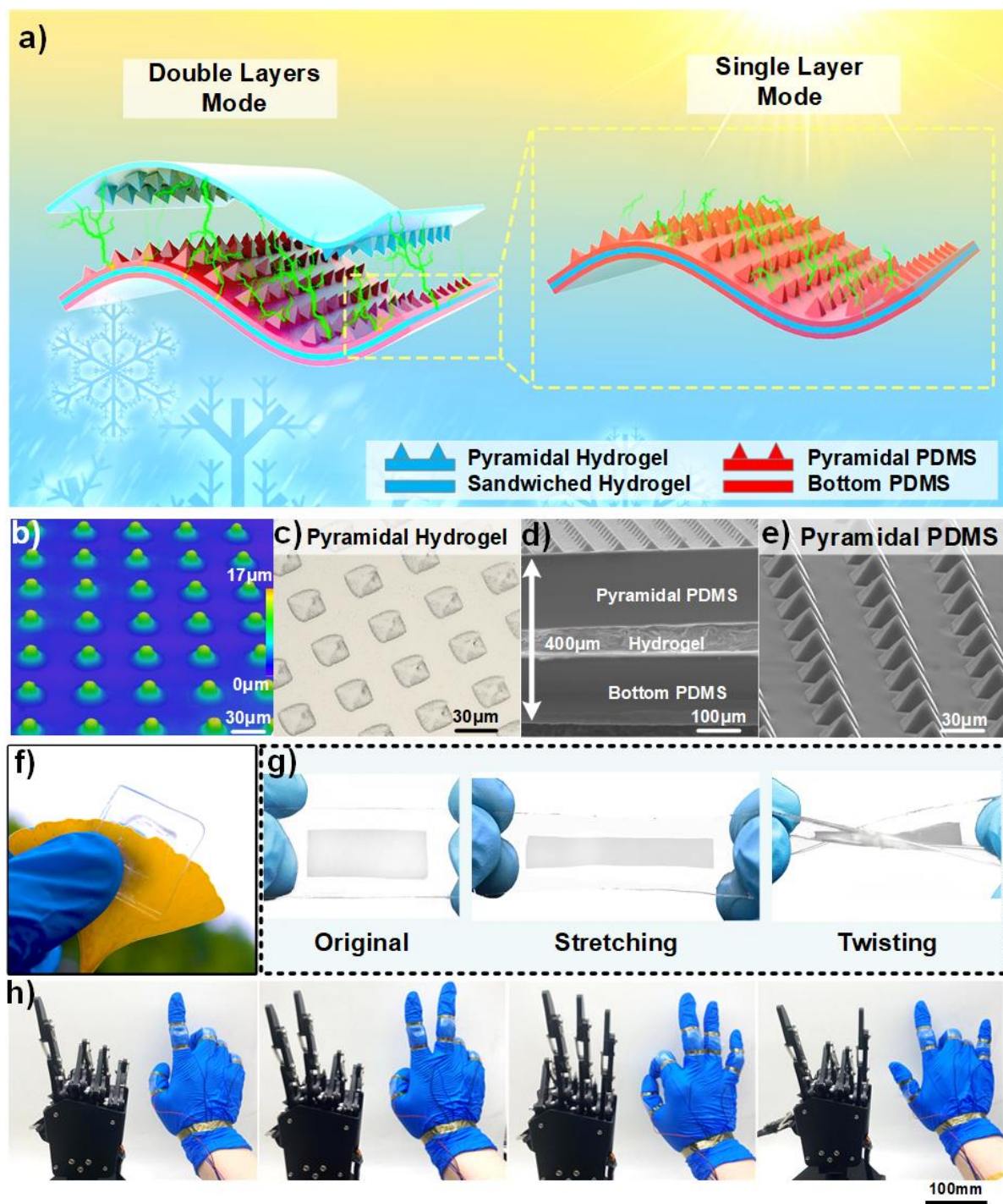


Figure 1.

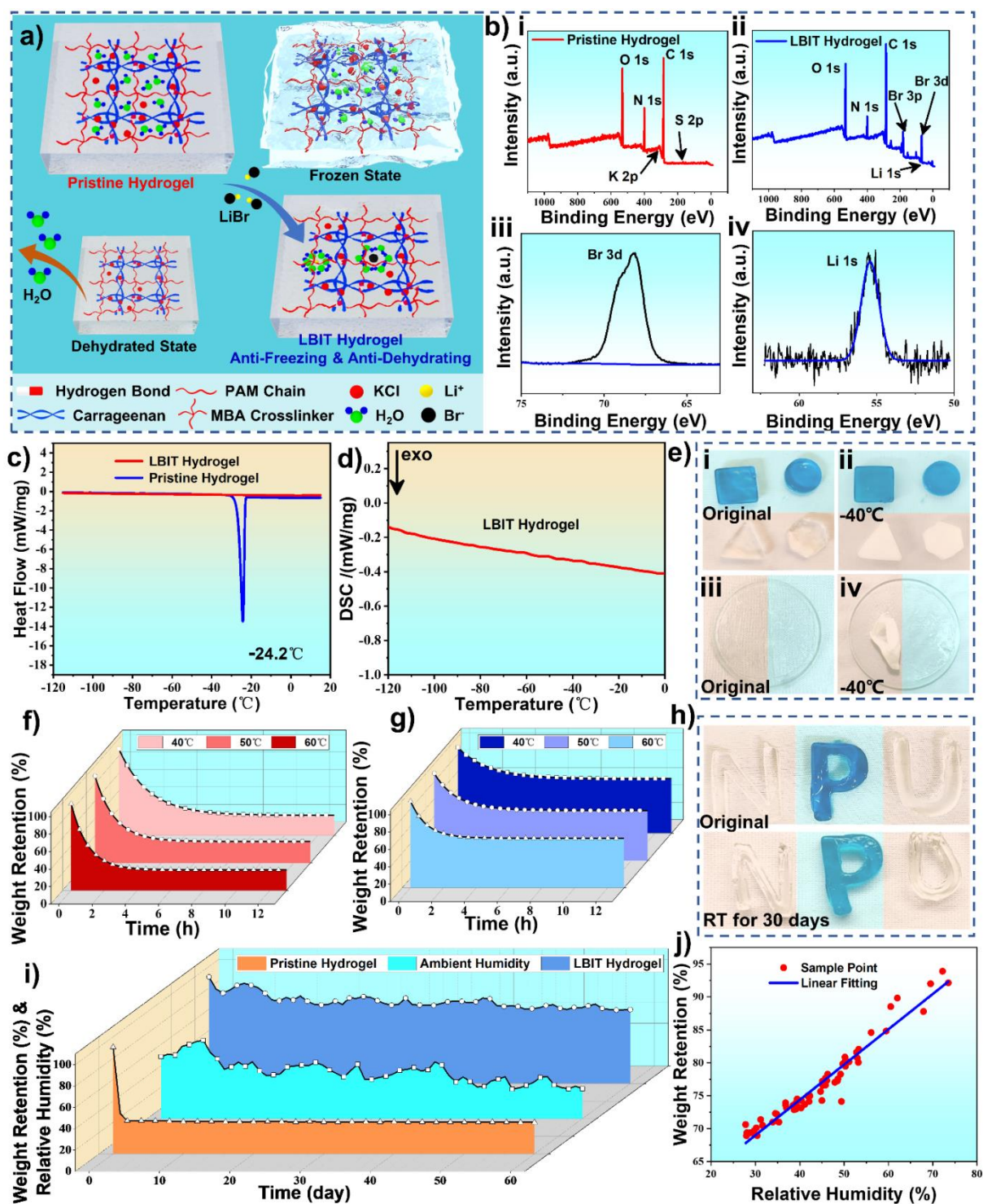


Figure 2.

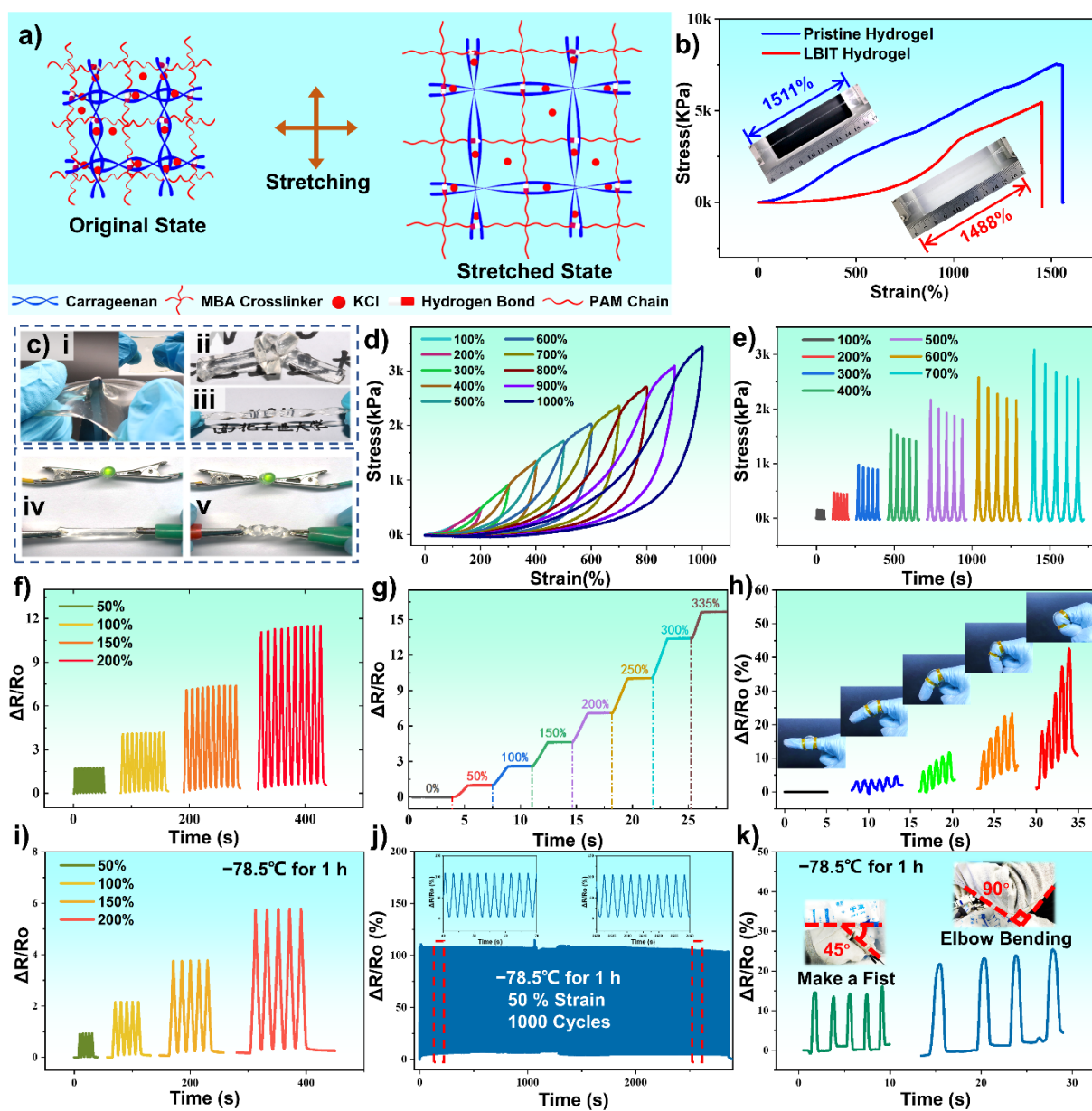


Figure 3.

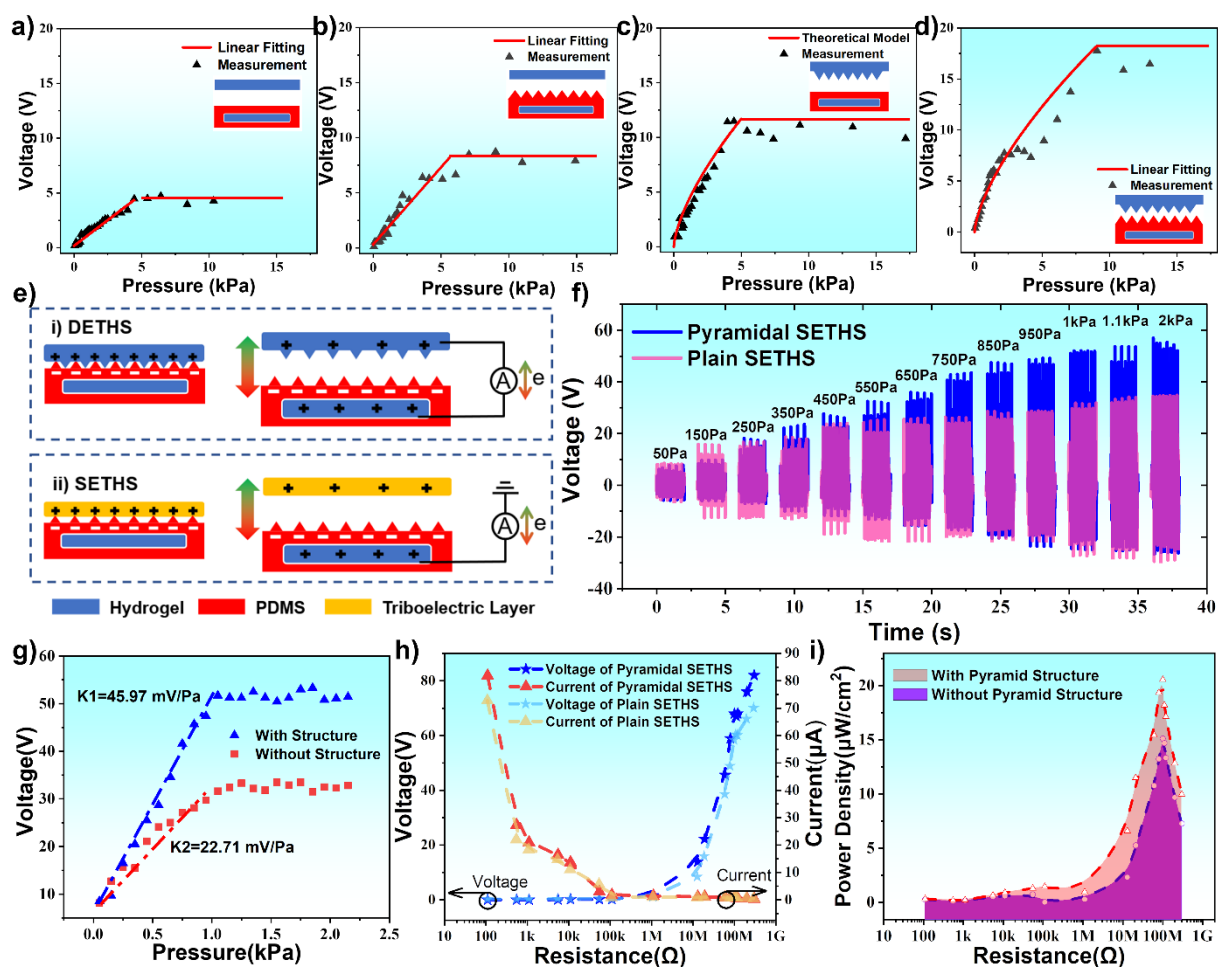


Figure 4.

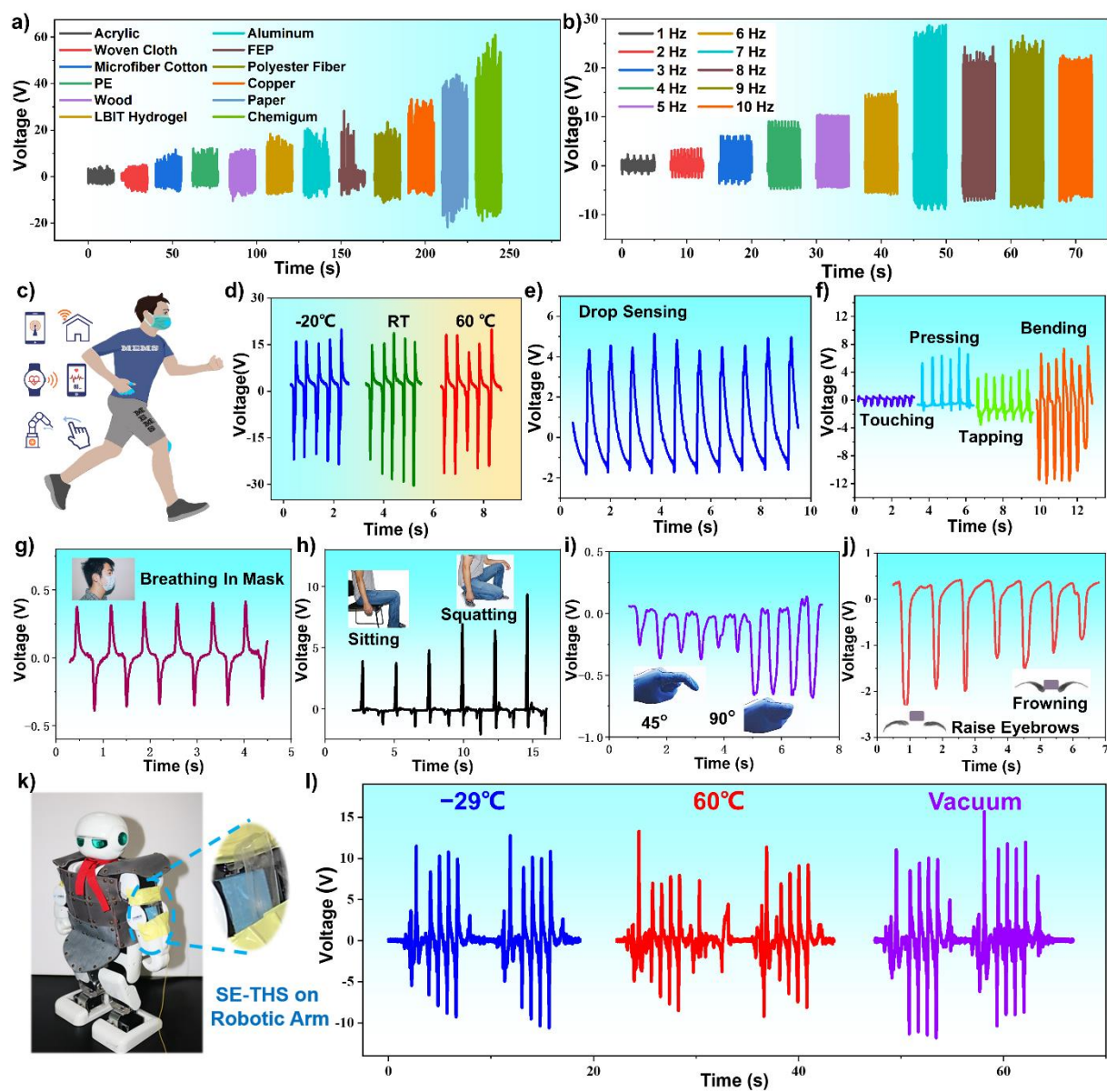


Figure 5.

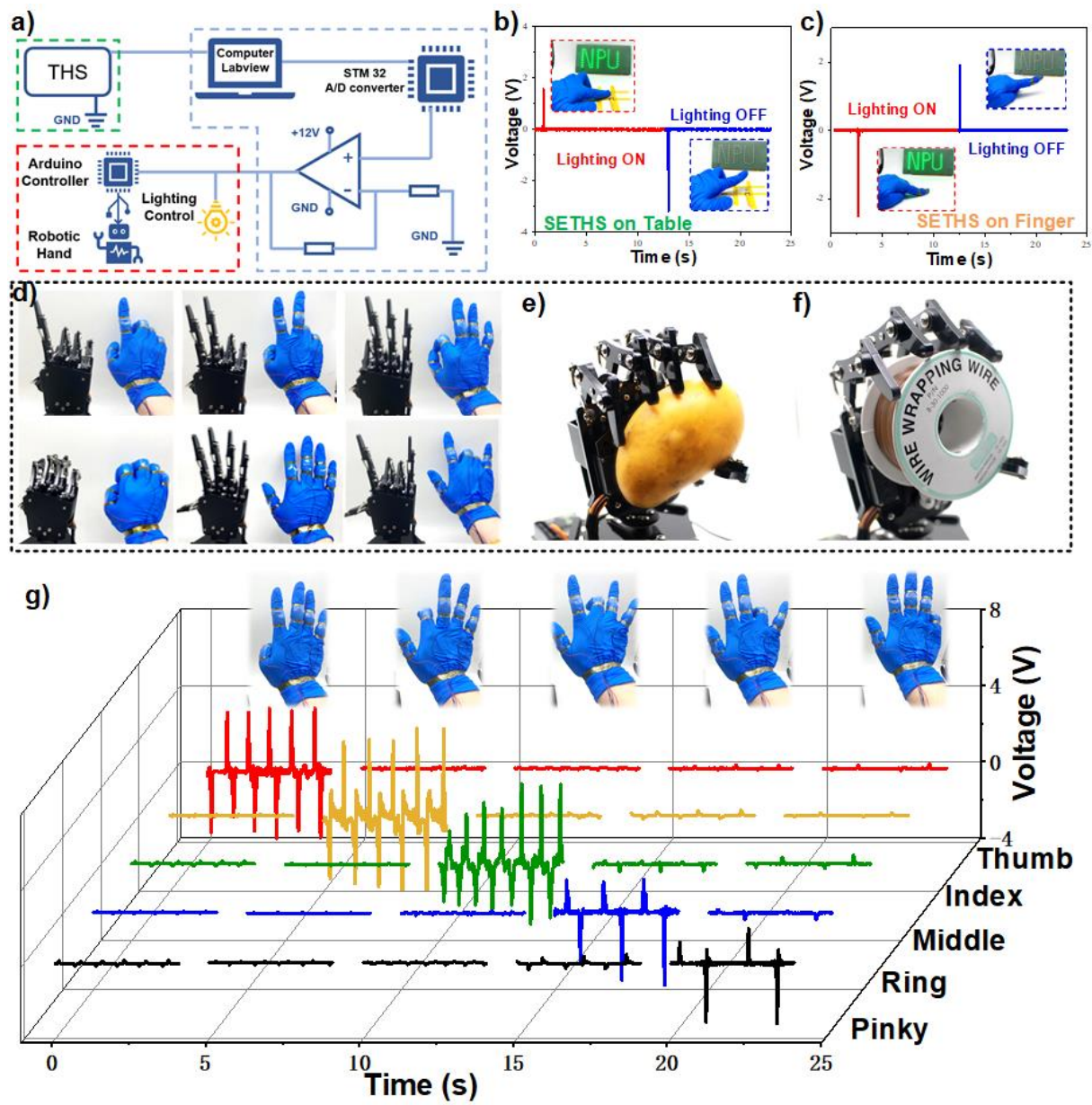


Figure 6.